Supporting Information

Efficient ammonia synthesis via electrocatalytic nitrate reduction over a [8+2]-connected three-dimensional metal–bipyridine covalent organic framework

Tsukasa Irie,[a,+] Ayumu Kondo,[a,+] Kai Sun,[b,+] Kohki Sasaki,[a] Mika Nozaki,[a] Shiho Tomihari,[a] Kotaro Sato,[c] Tokuhisa Kawawaki,[a] Yu Zhao,*[d] Saikat Das,*[a] and Yuichi Negishi*[a]

[a]Institute of Multidisciplinary Research for Advanced Materials, Tohoku University, 2-1-1 Katahira, Aoba-ku, Sendai 980-8577, Japan

[b]Department School of Materials and Energy, and LONGi Institute of Future Technology, Lanzhou University, Lanzhou 730000, China

[c]Carbon Value Research Center, Research Institute for Science & Technology, Tokyo University of Science, Kagurazaka, Shinjuku−ku, Tokyo 162−8601, Japan

[d]Zhejiang Engineering Laboratory for Green Syntheses and Applications of Fluorine-Containing Specialty Chemicals, Institute of Advanced Fluorine-Containing Materials, Zhejiang Normal University, 321004 Jinhua, China

[+]These authors contributed equally

*Corresponding Author
Y.Z.: zhaoyu@zjnu.edu.cn
S.D.: das.saikat.c4@tohoku.ac.jp
Y.N.: yuichi.negishi.a8@tohoku.ac.jp

Table of Contents

1. Materials and Methods

1.1. Chemicals. Unless stated otherwise, all chemicals and solvents, were of analytical grade and used as received without additional purification. Anhydrous *o*-dichlorobenzene, *n*-butanol, acetic acid (AcOH), and tetrahydrofuran (THF) were obtained from FUJIFILM Wako Pure Chemical Corporation. Sodium hypochlorite pentahydrate ($NaClO{\cdot}5H_2O$), *N*-(1-naphthyl)ethyldiamine dihydrochloride ($C_{10}H_7NHCH_2CH_2NH_2{\cdot}2HCl$), and salicylic acid ($C_6H_4(OH)COOH$) were obtained from Tokyo Chemical Industry Co., Ltd. 2-propanol, Nafion®, deuterium oxide (D_2O), sodium hydroxide (NaOH), sodium citrate ($Na_3C_6H_5O_7$), sodium nitroferricyanide ($C_5FeN_6Na_2O$), sulfanilamide ($H_2NC_6H_4SO_2NH_2$), phosphoric acid (H_3PO_4), 50% potassium hydroxide solution (KOH), potassium nitrite (KNO_2), potassium nitrate (KNO_3), and potassium thiocyanate (KSCN) were obtained from FUJIFILM Wako Pure Chemical Corporation. Methanol (MeOH) and hydrochloric acid (HCl) were obtained from Kanto Chemical Co., Inc. Isotope KNO_3 ($K^{15}NO_3$) was obtained from Sigma-Aldrich Co. Carbon black (Vulcan XC-72) was obtained from Fuel Cell Earth and carbon paper (SIGRACET®; GDL 22BB) was obtained from SGL carbon. Pure Milli-Q water (>18 MΩ × cm) was generated using a Merck Millipore Direct 3 UV system.

1.2. Characterization.

Powder X-ray diffraction (PXRD): PXRD patterns were recorded on a Rigaku MiniFlex X-ray diffractometer with a CuKα source (λ = 1.5418 Å), operated at 40 kV and 15 mA. The diffraction data were collected over a 2θ range of 3–40°, with a step size of 0.01° and a scanning speed of 2.8° per minute.

Fourier transform infrared (FT-IR) spectroscopy: FT-IR spectra were obtained on a JASCO FT/IR-6600 FT-IR spectrometer over the wavenumber range of 4000–400 cm^{-1} using the KBr pellet technique.

Solid-state ^{13}C cross-polarization magic-angle-spinning (CP-MAS) NMR spectroscopy: The solid-state NMR spectra were recorded using a Bruker Biospin Avance III 600 NMR spectrometer equipped with a 4-mm probe at a spinning rate of 10 kHz.

Scanning electron microscopy (SEM): SEM images and corresponding EDX elemental maps were acquired on a JEOL JSM-7800F field emission scanning electron microscope equipped with an Oxford X-Max EDX detector at an accelerating voltage of 15 kV. Prior to imaging, a thin Pt layer was sputter-coated onto the samples to minimize charging.

Transmission electron microscopy (TEM): HR-TEM images and corresponding fast Fourier transform (FFT) patterns were acquired using a FEI Tecnai F30 transmission electron microscope.

X-ray photoelectron spectroscopy (XPS): XPS measurements were carried out on a JPS-9-1-MC electron spectrometer (JEOL, Tokyo, Japan) with Mg K_α radiation (1253.6 eV) as the excitation source.

High-angle annular dark-field scanning transmission electron microscopy (HAADF-STEM): HAADF-STEM imaging was performed using an ultra-high-resolution transmission electron microscope (Thermo Fisher Titan Themis Z G2 300) operating at 300 kV, with a beam convergence semi-angle of 25 mrad and HAADF collection angle from 39−200 mrad.

Inductively coupled plasma mass spectrometry (ICP-MS): ICP-MS analysis was carried out using an Agilent 7800 ICP-MS instrument. The operating conditions were as follows: peristaltic pump rate, 20 rpm; nebulizer gas flow rate, 1.0 L min^{-1}; auxiliary gas flow rate, 1.0 L min^{-1}; sample flush time, 40 s; and radio frequency (RF) power, 1550 W.

Prior to analysis, samples were digested in an appropriate acid mixture and diluted to a final volume (V_0, in mL). The measured concentration of the target element in the test solution (C_0, in μg/L) was corrected for dilution (factor *f*) to obtain the concentration in the original digest solution (C_1), according to:

$$C_1(\mu g/L) = C_0(\mu g/L) \times f$$

The final elemental content in the solid sample (C_x, in μg/kg) was calculated using the following equation:

$$C_x(\mu g/kg) = \frac{C_1(\mu g/L) \times V_0(mL) \times 10^{-3}}{m(g) \times 10^{-3}}$$

where m is the mass of the solid sample used for digestion (in g). The reported value C represents the average of three independent measurements of C_x for each sample.

Nitrogen sorption: Nitrogen sorption isotherms were measured at 77 K using a Quantachrome Autosorb iQ3 gas sorption analyzer. Before measurements, the pristine and metalated COF samples were degassed at 100 °C for 8 h using a turbomolecular vacuum pump. The specific surface areas were determined from the nitrogen adsorption data using the multipoint Brunauer–Emmett–Teller (BET) method. Pore size distributions were obtained from the adsorption branch of the isotherm using quenched solid density functional theory (QSDFT), assuming a cylindrical pore model.

Thermogravimetric analysis (TGA): TGA data were collected on a Thermo plus EVO2 thermal analyzer by heating the samples from room temperature to 800 °C under a nitrogen atmosphere, using a ramp rate of 10 °C min^{-1} and nitrogen flow rate of 50 mL min^{-1}.

Elemental analyses: Elemental analysis of the COF was performed with a Micro Corder JM10 elemental analyzer.

X-ray absorption fine structure (XAFS): XAFS measurements were carried out at the BL14W1 beamline of the Shanghai Synchrotron Radiation Facility (SSRF), China. A Si(111) double-crystal monochromator was used to monochromatize the incident X-ray beam. Before the measurements, the powder samples were pressed into thin sheets (~1 cm in diameter), enclosed in PTFE sample holders, and sealed with 3M Scotch tape to prevent contamination and air exposure. Fe K-edges of XAFS spectra were collected for TU-82-Fe, Fe foil, FeO, Fe_2O_3, and iron phthalocyanine (FePc), while Cu K-edges of XAFS spectra were measured for TU-82-Cu, Cu foil, Cu_2O, CuO, and copper phthalocyanine (CuPc). Data reduction, analysis, and extended XAFS (EXAFS) fitting were performed using the Athena and Artemis programs within the Demeter software package[1], which employs the FEFF6 program[2] to fit the EXAFS data. Energy calibration was carried out using standard Fe and Cu foils, which were measured simultaneously with the samples as internal references. A linear function was subtracted from the pre-edge region, then the edge jump was normalized using Athena software. The χ(k) data were extracted by subtracting a smooth, third-order polynomial approximating the absorption background of an isolated atom. The k^3-weighted χ(k) data were Fourier transformed after applying a Hanning window function (Δk = 1.0). EXAFS modeling was conducted in R-space using Artemis, where structural parameters—coordination number (CN), the distance between absorber and backscatter atoms (R), Debye–Waller factor (σ^2), and inner potential correction (ΔE_0)—were obtained via nonlinear least-squares fitting of the Fourier-transformed EXAFS equation. The amplitude reduction factors (S_0^2) were determined from fitting the reference Fe and Cu foil data and fixed at 0.740 and 0.828, respectively, during subsequent fitting of the sample spectra to estimate coordination numbers (CNs).

Wavelet transform analysis was performed using the Hama Fortran code, with χ(k) data exported from Athena as input. The following parameters were applied: R range = 1–4 Å, k range = 0–15 $Å^{-1}$, and k-weight = 3. The Morlet wavelet function with κ = 10 and σ = 1 was used as the mother wavelet to provide the overall distribution.

1.3. Synthesis of building blocks. 4′,5′-bis(3,5-diformylphenyl)-3′,6′-dimethyl-[1,1′:2′,1″-terphenyl]-3,3″,5,5″-tetracarbaldehyde (DPTB-Me)[3] and 2,2′-bipyridine-5,5′-diamine (Bpy)[4] were synthesized following previous literature.

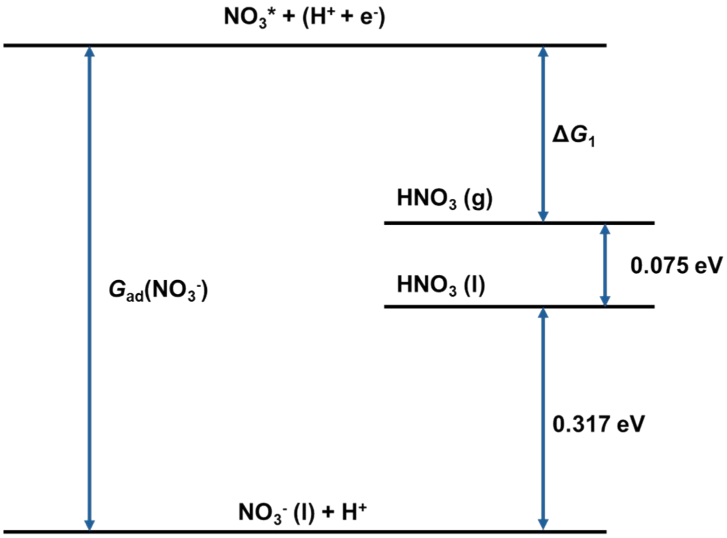

Figure S1. Schematic depiction of the thermodynamic cycle used to calculate the adsorption free energy of NO_3^- ($G_{ad}(NO_3^-)$). This figure is adapted from references 5 and 6, with thermodynamic data sourced from the CRC Handbook of Chemistry and Physics[7].

2. PXRD analysis of metalated COFs

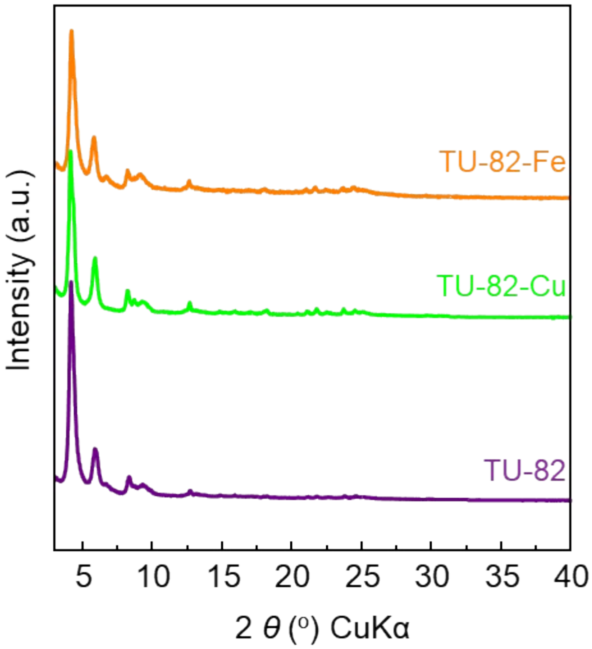

Figure S2. PXRD profiles of TU-82, TU-82-Fe, and TU-82-Cu.

3. Solid-state ^{13}C CP-MAS Nuclear Magnetic Resonance (NMR) spectroscopy

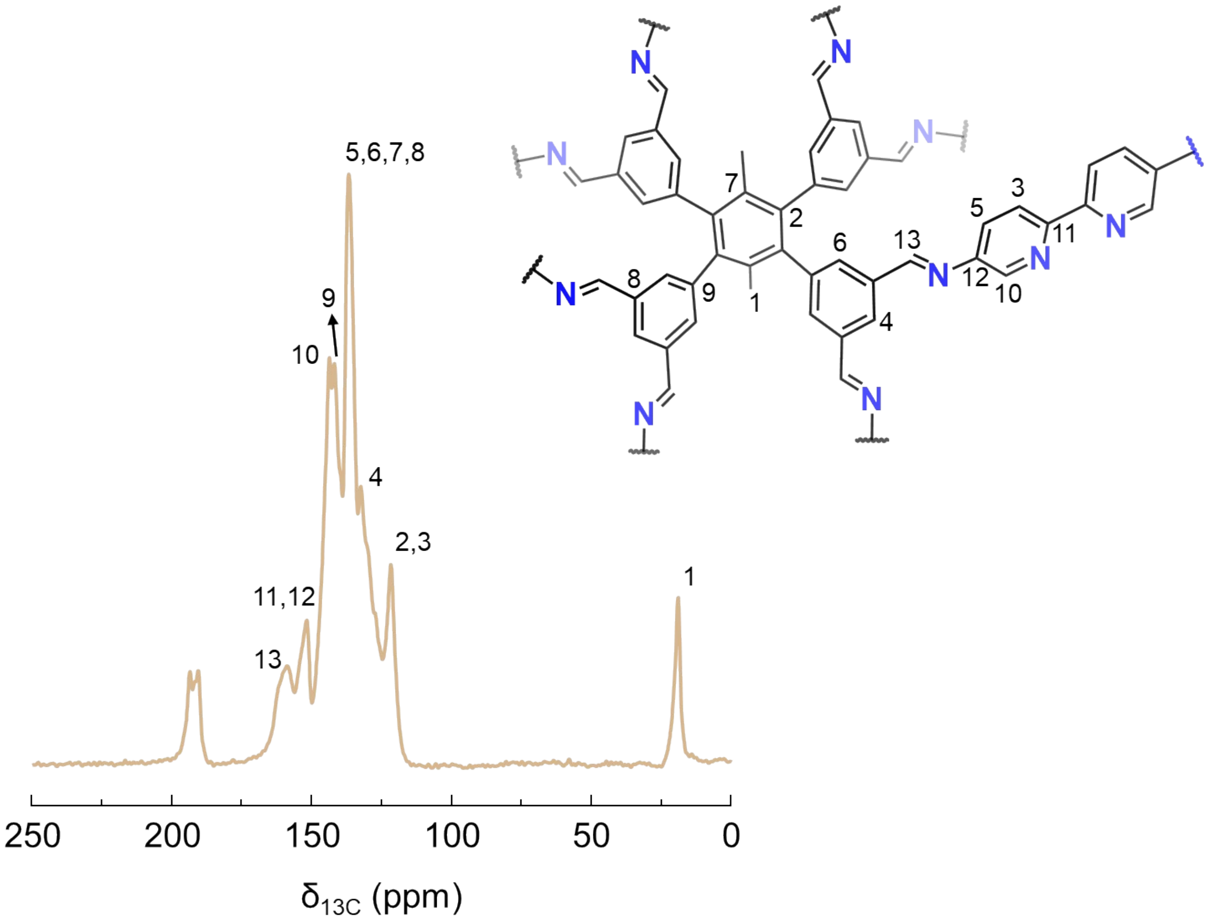

Figure S3. Solid-state ^{13}C CP-MAS NMR spectrum of TU-82. The asterisk denotes spinning sidebands.

4. BET surface area plot

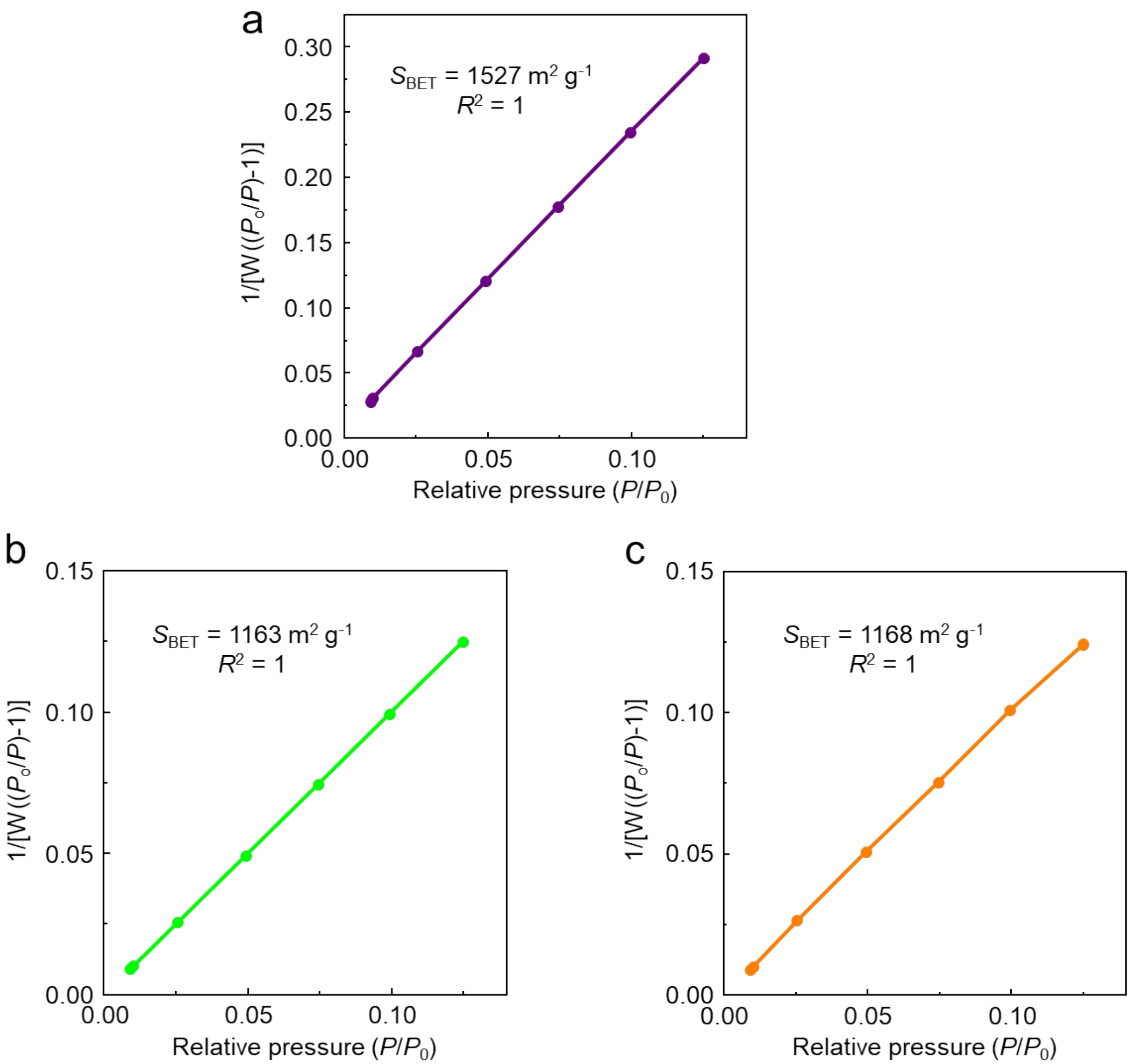

Figure S4. BET plots for (a) TU-82, (b) TU-82-Cu, and (c) TU-82-Fe derived from N_2 adsorption isotherms measured at 77 K. The BET surface areas (S_{BET}) were calculated to be 1857, 1163, and 1168 m^2 g^{-1} for TU-82, TU-82-Cu, and TU-82-Fe, respectively. All BET fits yielded a correlation coefficient of $R^2 = 1$.

5. Scanning electron microscopy (SEM) and transmission electron microscopy (TEM) characterization

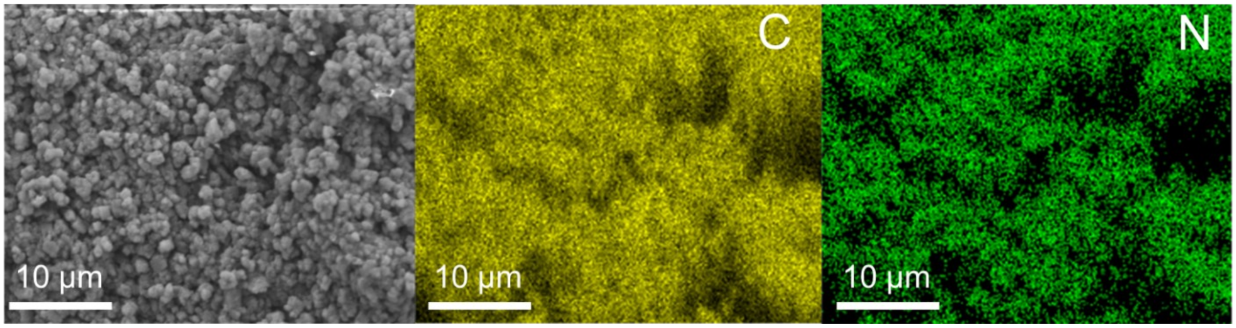

Figure S5. SEM image of TU-82 and corresponding EDX elemental maps for carbon and nitrogen.

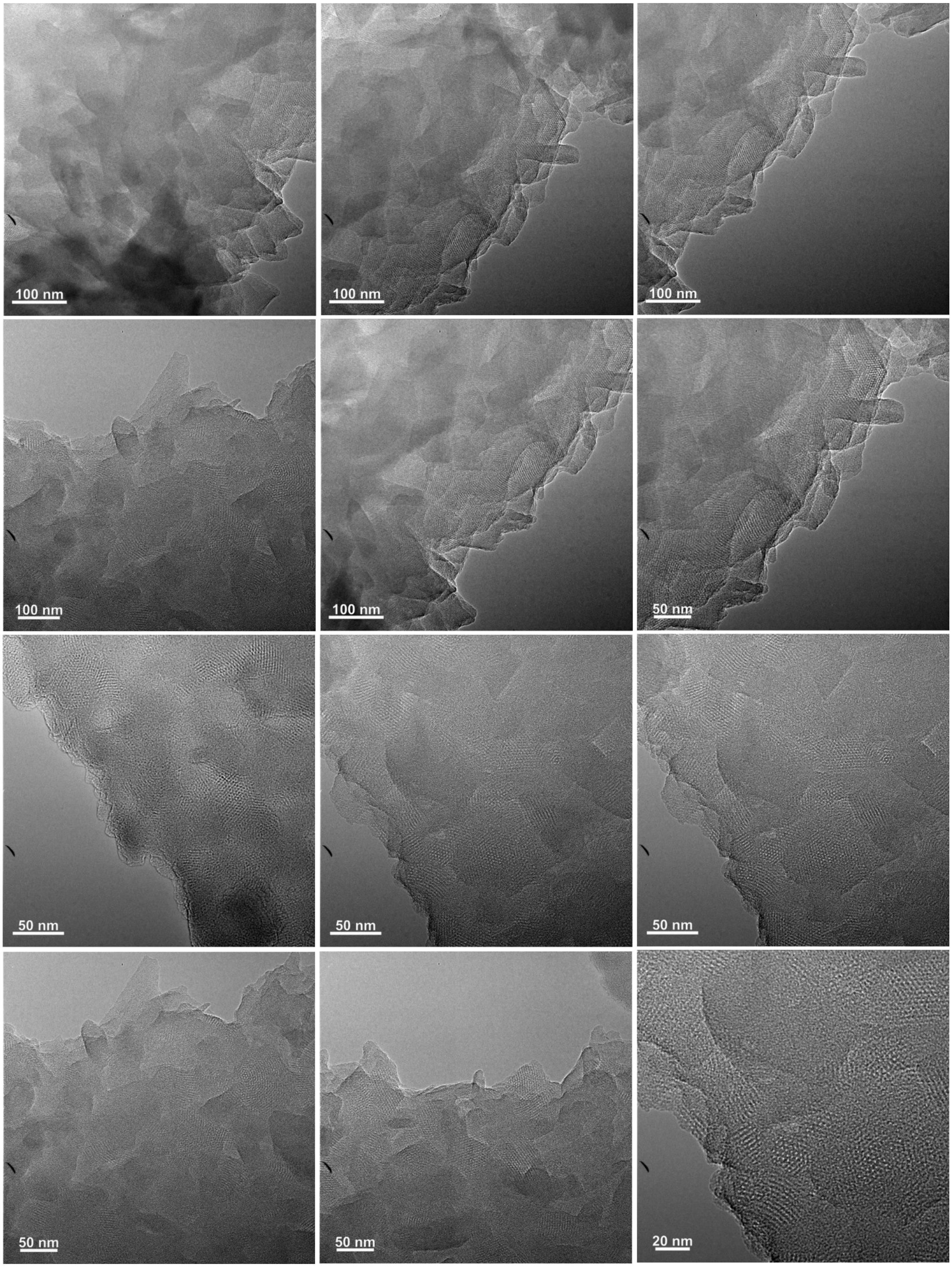

Figure S6. HR-TEM images of TUS-39.

6. Inductively coupled plasma mass spectrometry (ICP-MS)

Table S1. Quantitative metal content in TU-82-Fe and TU-82-Cu determined by ICP-MS, based on three independent measurements.

Samples	m (in g)	V_0 (in mL)	Test elements	C_0 (in µg/L)	*f*	C_1 (in µg/L)	C_x (in µg/kg)	Element content (wt%)	Average wt%
TU-82-Fe	0.0226	25	Fe	57.5962552	1000	57596.255	63712671.681	6.37	6.42
TU-82-Fe	0.0226	25	Fe	58.5120063	1000	58512.006	64725670.686	6.47	
TU-82-Fe	0.0226	25	Fe	58.0304263	1000	58030.426	64192949.447	6.42	
TU-82-Cu	0.0166	25	Cu	59.6872679	1000	59687.268	89890463.705	8.99	8.95
TU-82-Cu	0.0166	25	Cu	59.5208563	1000	59520.856	89639843.825	8.96	
TU-82-Cu	0.0166	25	Cu	59.0699584	1000	59069.958	88960780.723	8.90	

7. Thermogravimetric analysis (TGA)

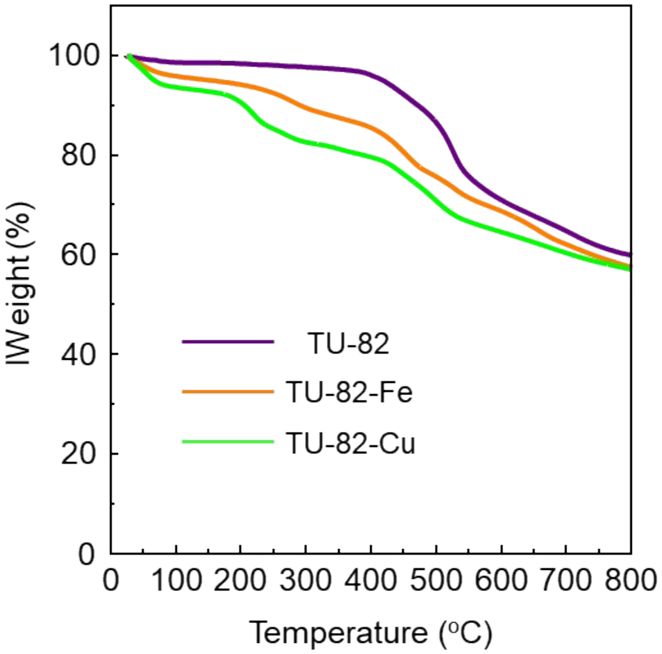

Figure S7. TGA curves of TU-82, TU-82-Fe, and TU-82-Cu under N_2 atmosphere.

8. Chemical stability analysis

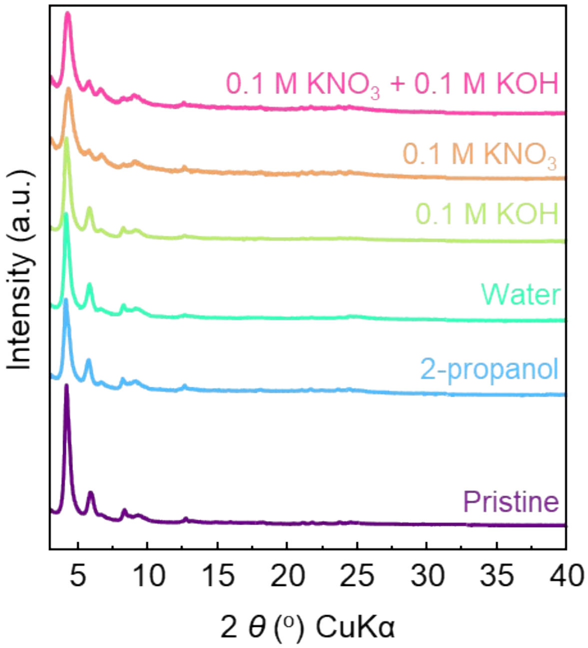

Figure S8. PXRD profiles of TU-82 after immersing in different solvents for 24 hours.

9. Simulated structural model of TU-82

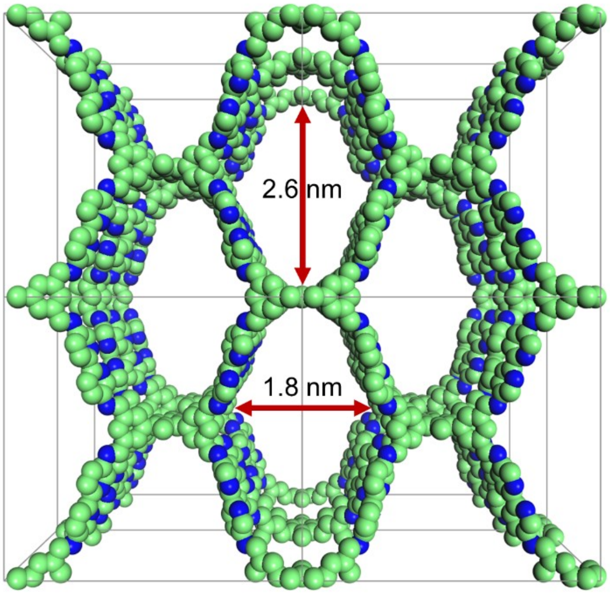

Figure S9. Space-filling model of TU-82, adopting a non-interpenetrated **bcu** topology within the *Imm2* space group. Pore metrics are highlighted. C, green; N, blue. H atoms are omitted for clarity.

10. X-ray photoelectron spectroscopy (XPS)

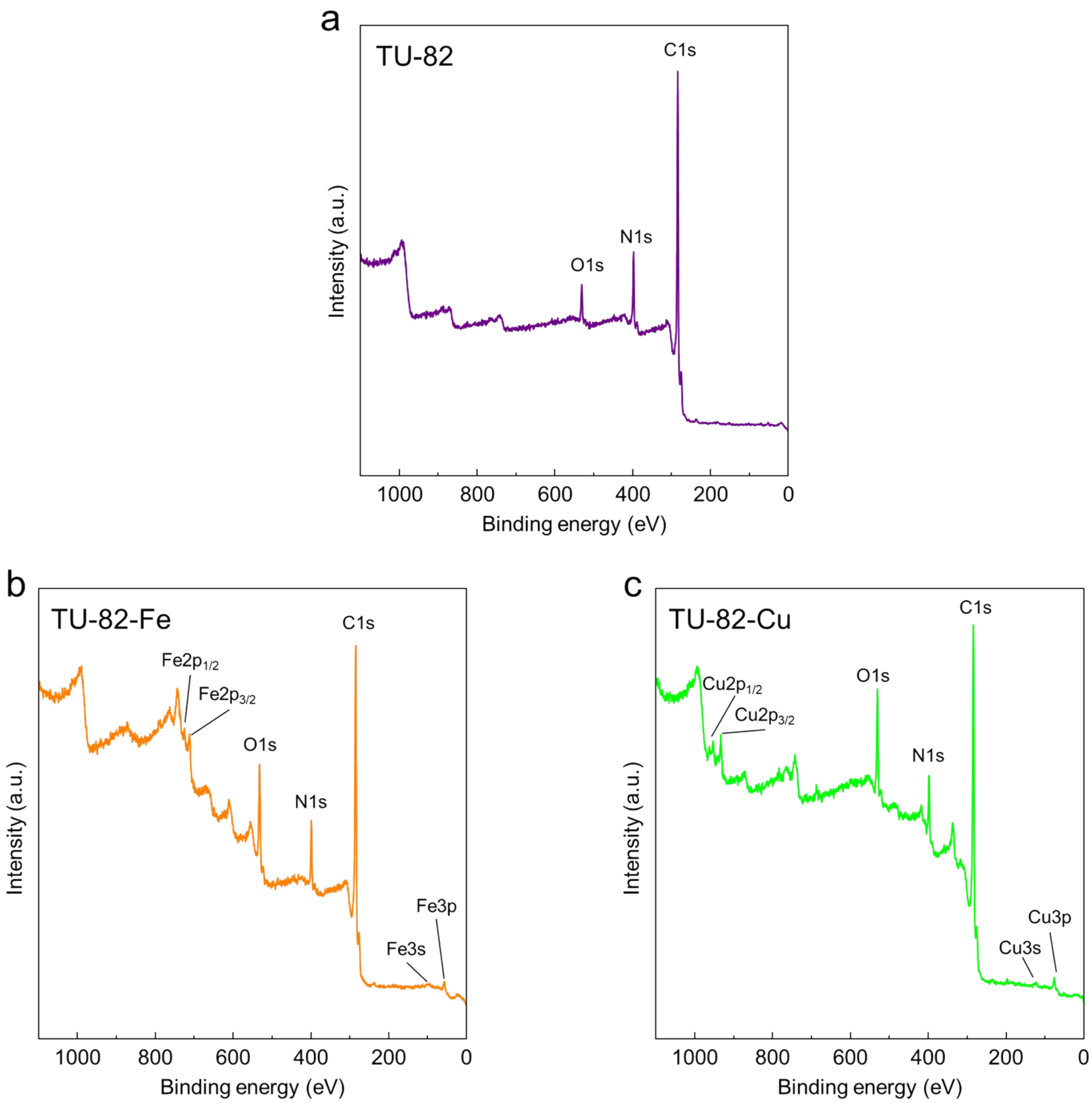

Figure S10. XPS survey spectra of (a) TU-82, (b) TU-82-Fe, and (c) TU-82-Cu.

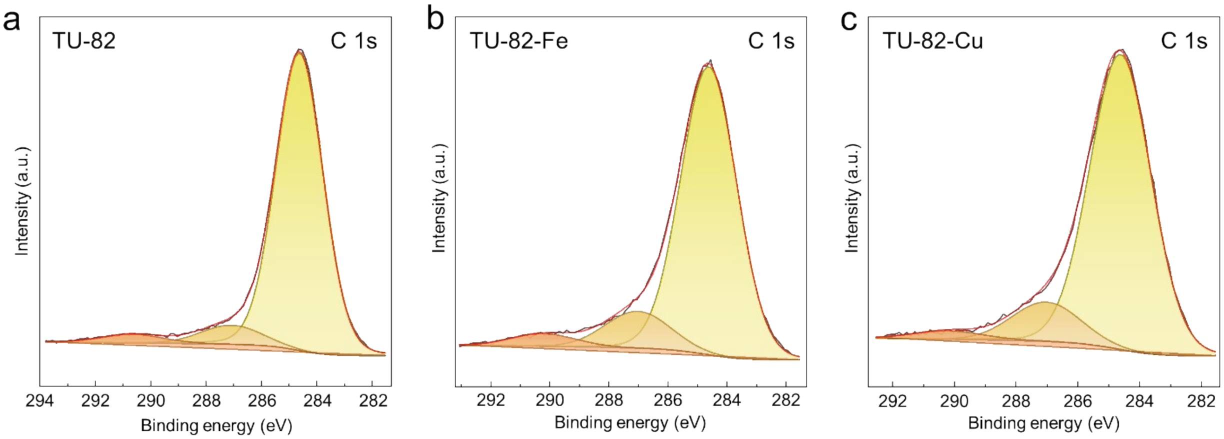

Figure S11. C1s XPS spectra and corresponding peak deconvolution for (a) TU-82, (b) TU-82-Fe, and (c) TU-82-Cu.

11. X-ray absorption near edge structure (XANES) analysis results

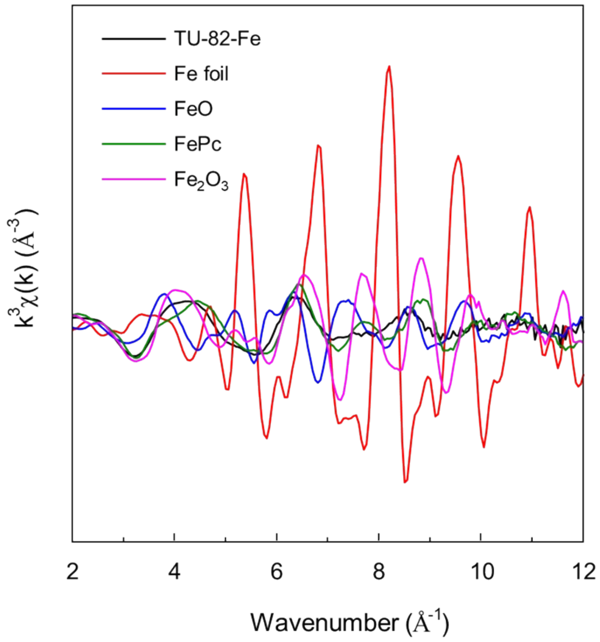

Figure S12. Fe K-edge extended X-ray absorption fine structure (EXAFS) spectra presented in k³-weighted k-space for TU-82-Fe and reference compounds. These correspond to the normalized XANES spectra shown in Figure 3d.

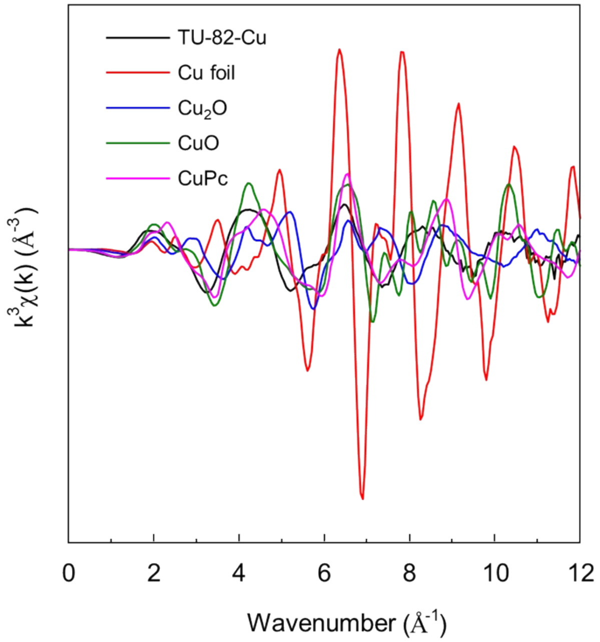

Figure S13. Cu K-edge extended X-ray absorption fine structure (EXAFS) spectra presented in k³-weighted k-space for TU-82-Cu and reference compounds. These correspond to the normalized XANES spectra shown in Figure 3h.

12. EXAFS fitting analysis results

Table S2. EXAFS fitting parameters at the Fe and Cu K-edge for various samples.

Sample	Shell	CN^a	R (Å)^b	σ^2 (Å^2)^c	ΔE_0 (eV)^d	k range/Å^{-1}	R range/Å	R factor
Fe K-edge								
Fe foil	Fe-Fe	8*	2.47±0.01	0.0050±0.0007	6.3±0.5	3.0–13.0	1.0–3.0	0.0069
	Fe-Fe	6*	2.84±0.01	0.0059±0.0009	5.3±0.8			
FeO	Fe-O	6*	2.14±0.01	0.0144±0.0020	1.7±0.5	3.0–11.0	1.0–3.2	0.0083
	Fe-Fe	12*	3.06±0.01	0.0122±0.0009	-1.7±0.4			
Fe_2O_3	Fe-O	6.0±0.6	1.98±0.01	0.0125±0.0020	-1.7±0.5	2.8–11.5	1.0–3.5	0.0033
	Fe-Fe	6.7±0.9	2.98±0.01	0.0085±0.0012	3.0±0.4			
	Fe-Fe	3.0±0.9	3.65±0.01	0.0021±0.0021	-9.6±0.8			
FePc	Fe-N	4.0±0.4	1.97±0.01	0.0053±0.0018	0.2±0.5	2.0–10.0	1.0–2.0	0.0084
TU-82-Fe	Fe-O/N	5.3±0.3	1.97±0.01	0.0099±0.0012	-1.9±0.3	2.5–12.0	1.0–2.0	0.0024
Cu K-edge								
Cu foil	Cu-Cu	12*	2.54±0.01	0.0086±0.0005	3.6±0.3	3.0–12.0	1.0-3.0	0.0043
Cu_2O	Cu-O	2*	1.84±0.01	0.0013±0.0008	6.6±0.6	3.0–12.0	1.0-3.5	0.0090
	Cu-Cu	12*	3.03±0.01	0.0193±0.0011	8.1±0.4			
	Cu-O	6*	3.55±0.01	0.0130±0.0042				
CuO	Cu-O	4.0±0.2	1.95±0.01	0.0036±0.0006	7.9±0.2	3.0–12.0	1.0–3.4	0.0019
	Cu-O	2.1±0.3	2.74±0.01					
	Cu-Cu	2.2±0.3	2.85±0.01	0.0045±0.0007	-5.6±0.7			
	Cu-Cu	2.3±0.3	3.39±0.01					
CuPc	Cu-N	4.0±0.6	1.94±0.01	0.0027±0.0014	8.4±1.2	3.2–13.0	1.2–2.0	0.0116
TU-82-Cu	Cu-O/N	4.1±0.2	1.95±0.01	0.0061±0.0008	3.0±0.2	2.5–12.0	1.0–2.0	0.0038

^{a}CN, coordination number; ^{b}R, the distance between absorber and backscatter atoms; $^c\sigma^2$, Debye-Waller factor to account for both thermal and structural disorders; $^d\Delta E_0$, inner potential correction; R factor indicates the goodness of the fit. S_0^2 was fixed to 0.740 and 0.828 respectively, according to the experimental EXAFS fit of Fe foil and Cu foil by fixing CN as the known crystallographic value.

*This value was fixed during EXAFS fitting. Error bounds that characterize the structural parameters obtained by EXAFS spectroscopy were estimated as CN ± 20%; R ± 1%; σ^2 ± 20%; ΔE_0 ± 20%. A reasonable range of EXAFS fitting parameters: $0.700 < S_0^2 < 1.000$; CN > 0; $\sigma^2 > 0$ Å^2; $|\Delta E_0| < 15$ eV; R factor < 0.02.

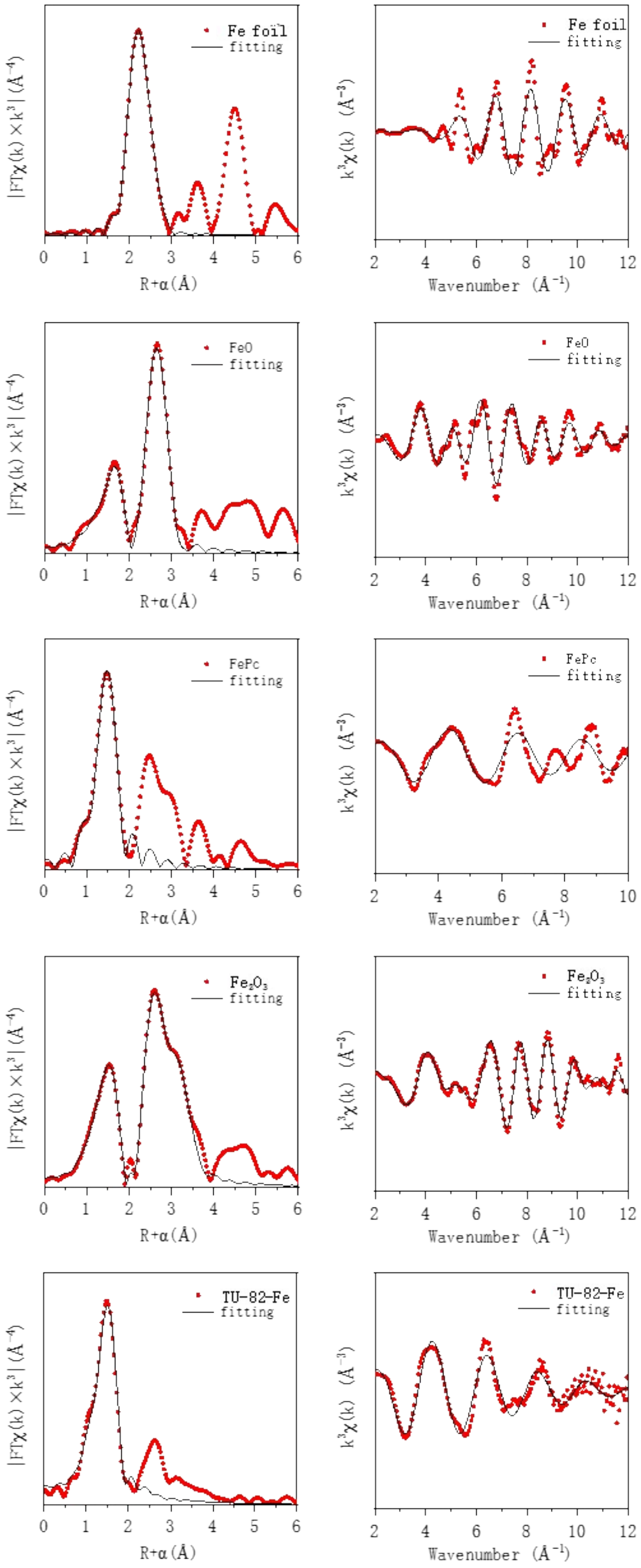

Figure S14. Fe K-edge EXAFS spectra (red) and corresponding fitting curves (black) for TU-82-Fe and reference materials, shown in k^3-weighted k-space (right) and R-space (left).

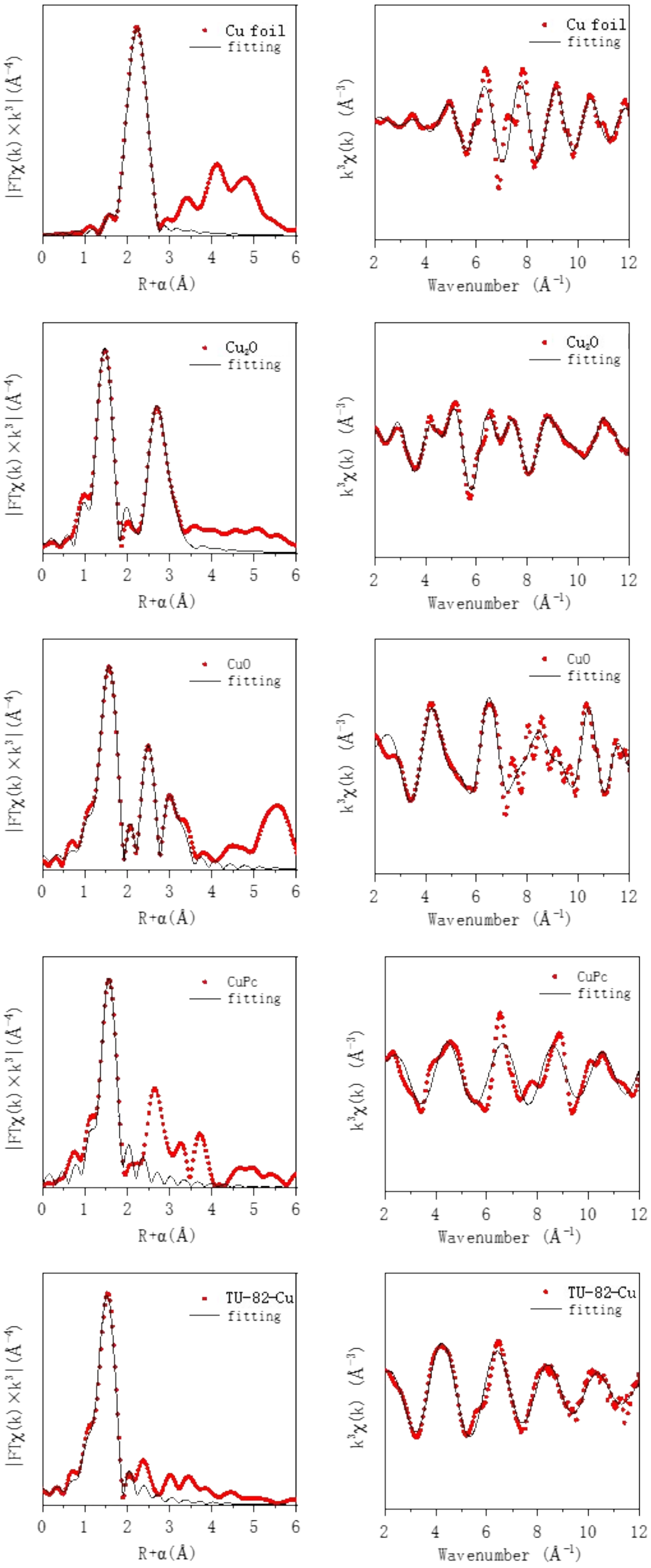

Figure S15. Cu K-edge EXAFS spectra (red) and corresponding fitting curves (black) for TU-82-Cu and reference materials, shown in k^3-weighted k-space (right) and R-space (left).

13. Electrochemical measurements

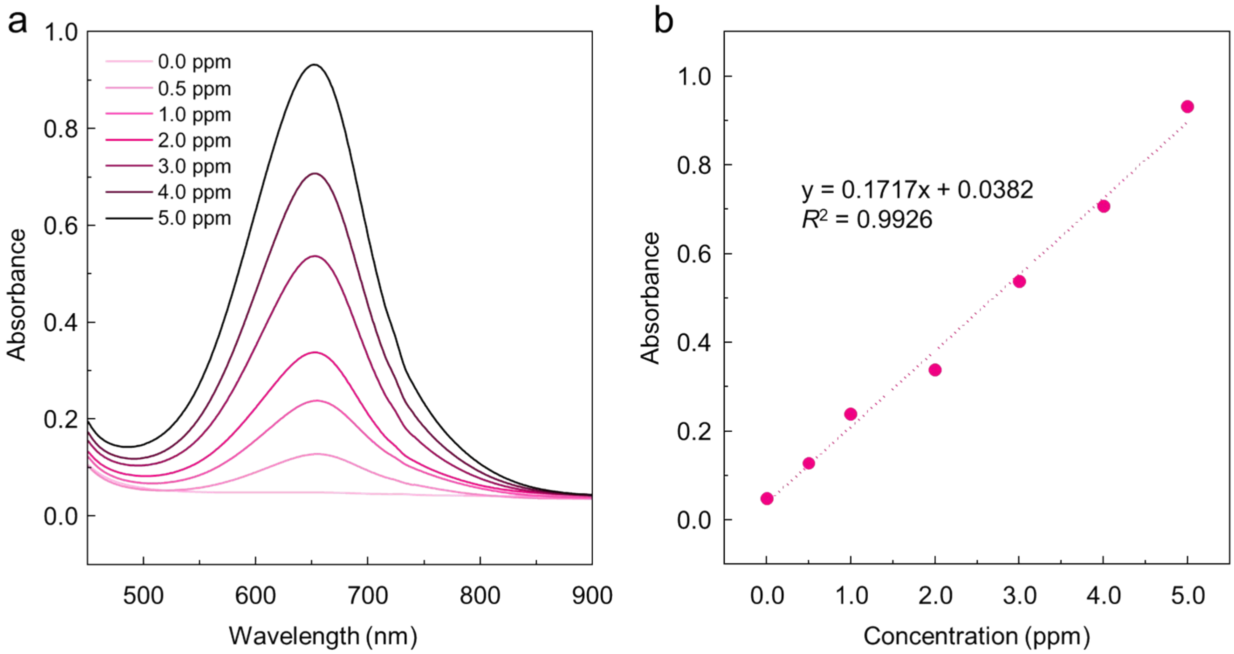

Figure S16. (a) UV–Vis absorption spectra and (b) corresponding calibration curves of the electrolyte with the given NH_3 concentrations.

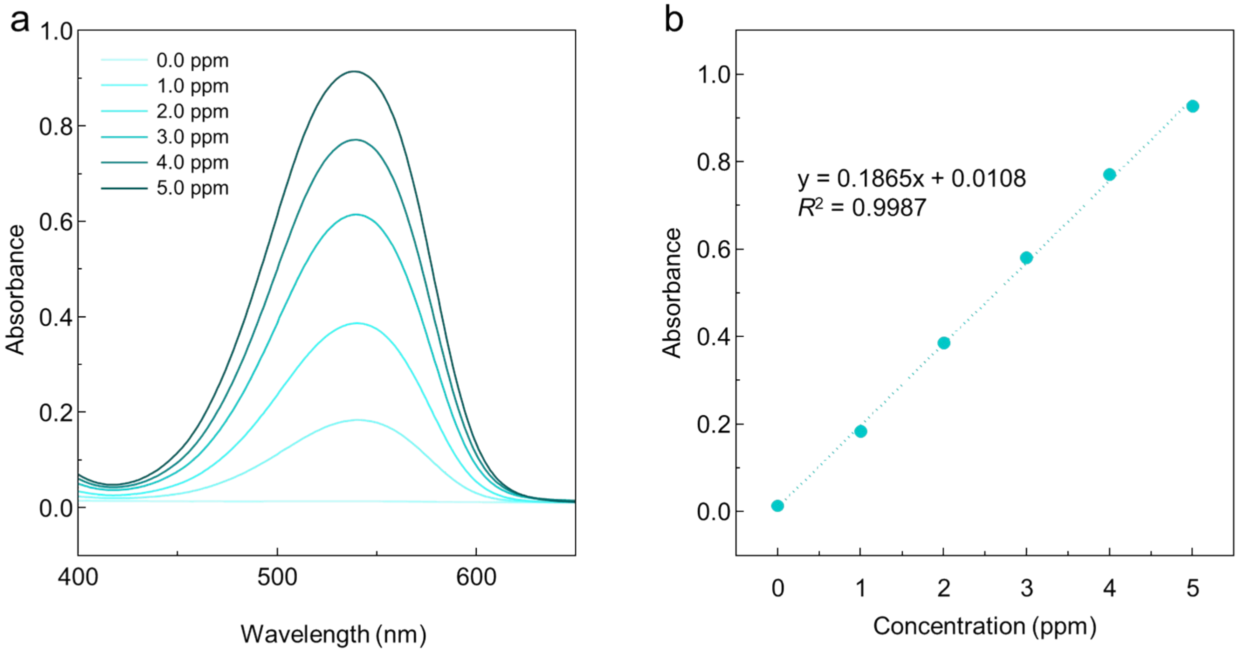

Figure S17. (a) UV–Vis absorption spectra and (b) corresponding calibration curves of the electrolyte with the given NO_2^- concentrations.

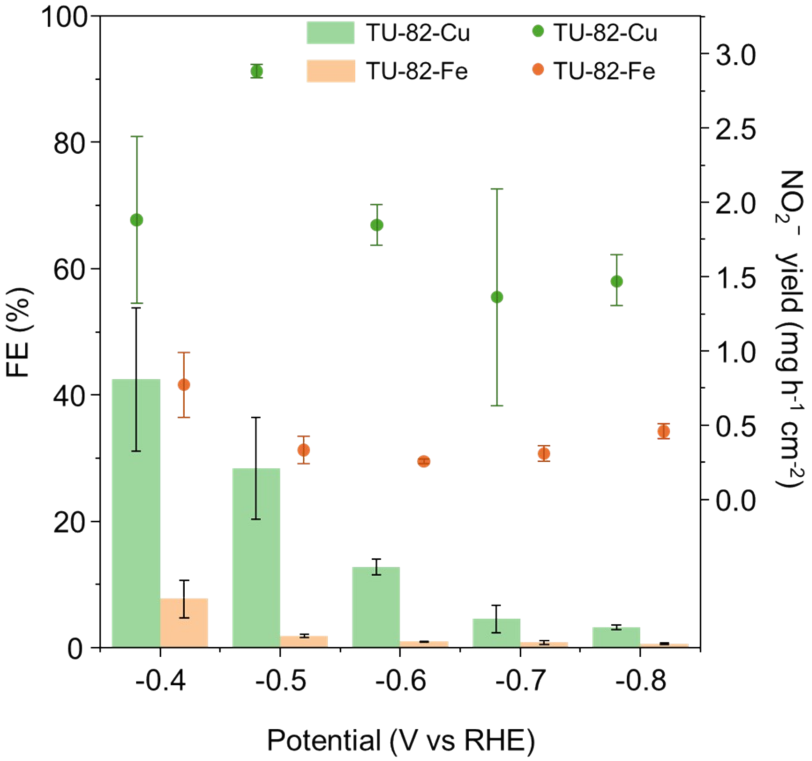

Figure S18. NO_2^- FE and yield rate for TU-82-Fe and TU-82-Cu at specific applied potentials. Error bars represent the standard deviation from three independent measurements.

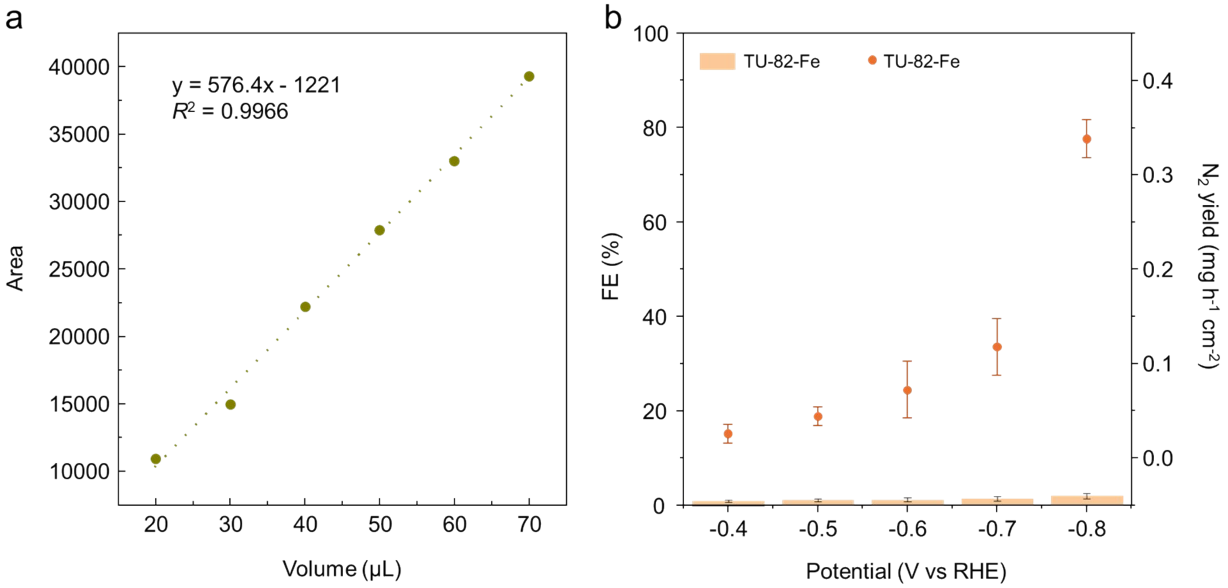

Figure S19. (a) Calibration curve for N_2 and (b) FE and yield rate of N_2 formation over TU-82-Fe at various applied potentials, measured by GC-TCD. Error bars represent the standard deviation from three independent measurements.

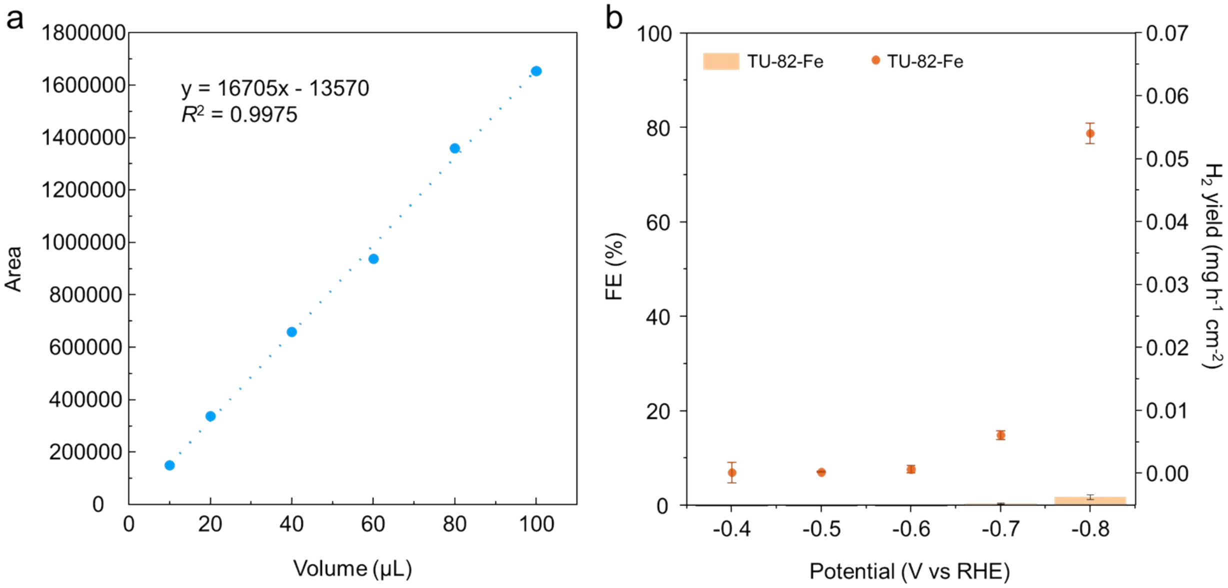

Figure S20. (a) Calibration curve for H_2 and (b) FE and yield rate of H_2 formation over TU-82-Fe at various applied potentials, measured by GC-TCD. Error bars represent the standard deviation from three independent measurements.

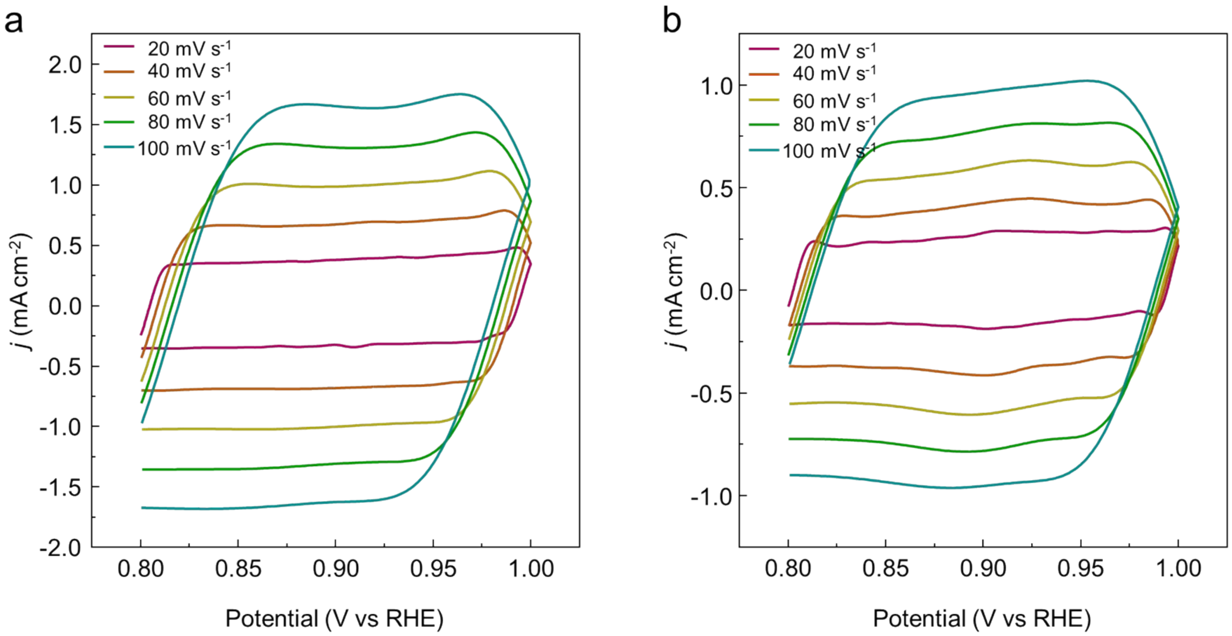

Figure S21. Cyclic voltammograms (CVs) recorded in the non-faradaic region at various scan rates for (a) TU-82-Fe and (b) TU-82-Cu. The electrochemical double-layer capacitance (C_{dl}), derived from these CVs, was used to estimate the electrochemical surface area (ECSA).

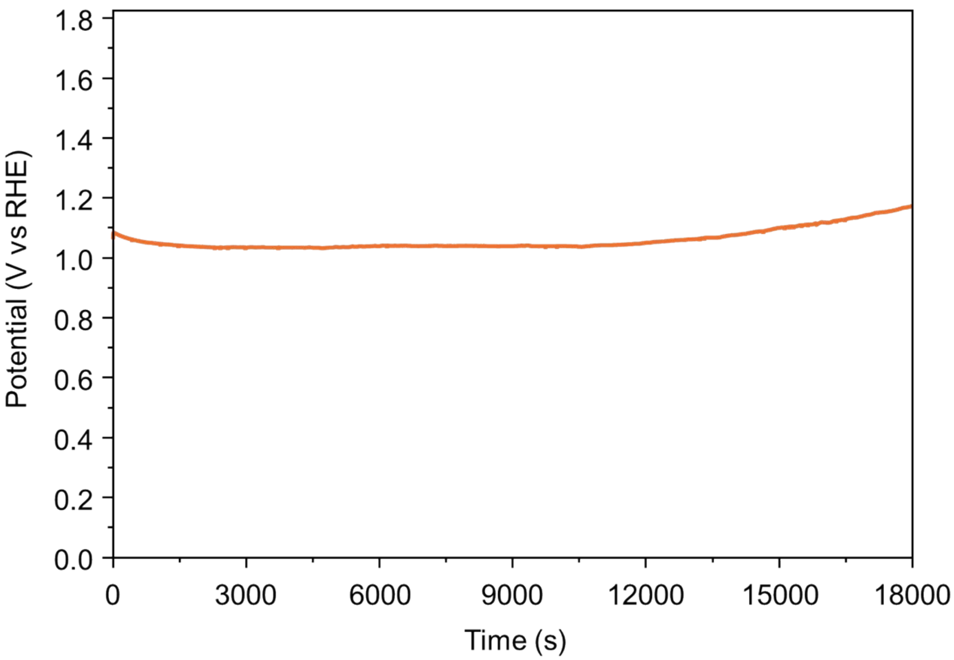

Figure S22. Chronopotentiometric (CP) stability profile of TU-82-Fe recorded in an aqueous electrolyte containing 0.5 M KNO_3 and 0.1 M KOH at a constant current density of 120 mA cm^{-2}. The potential was monitored as a function of time to evaluate the operational durability and electrochemical robustness of the catalyst under high-rate nitrate reduction conditions. The stable potential response throughout the measurement indicates that TU-82-Fe maintains efficient charge transport and structural integrity during sustained electrocatalysis, demonstrating its suitability for long-term NO_3RR operation at industrially relevant current densities.

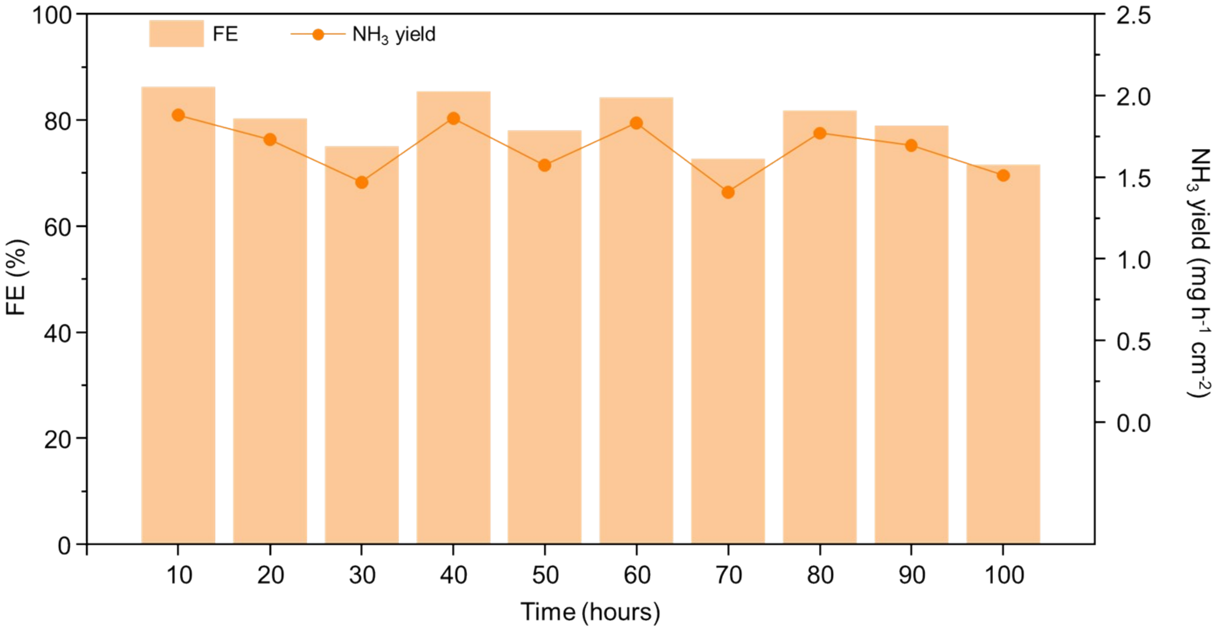

Figure S23. Long-term electrochemical stability assessment of TU-82-Fe conducted over 100 h at an applied potential of −0.6 V vs. RHE in alkaline nitrate-containing electrolyte. The time-dependent current response was continuously monitored to evaluate the catalyst's durability under sustained NO_3RR operating conditions. TU-82-Fe exhibits a stable catalytic profile with negligible current decay throughout the extended test, indicating robust active-site retention, efficient electron transport, and preservation of the framework integrity during prolonged electrocatalytic nitrate reduction. This long-duration performance highlights the structural and operational resilience of TU-82-Fe under practical, industrially relevant electrolysis conditions.

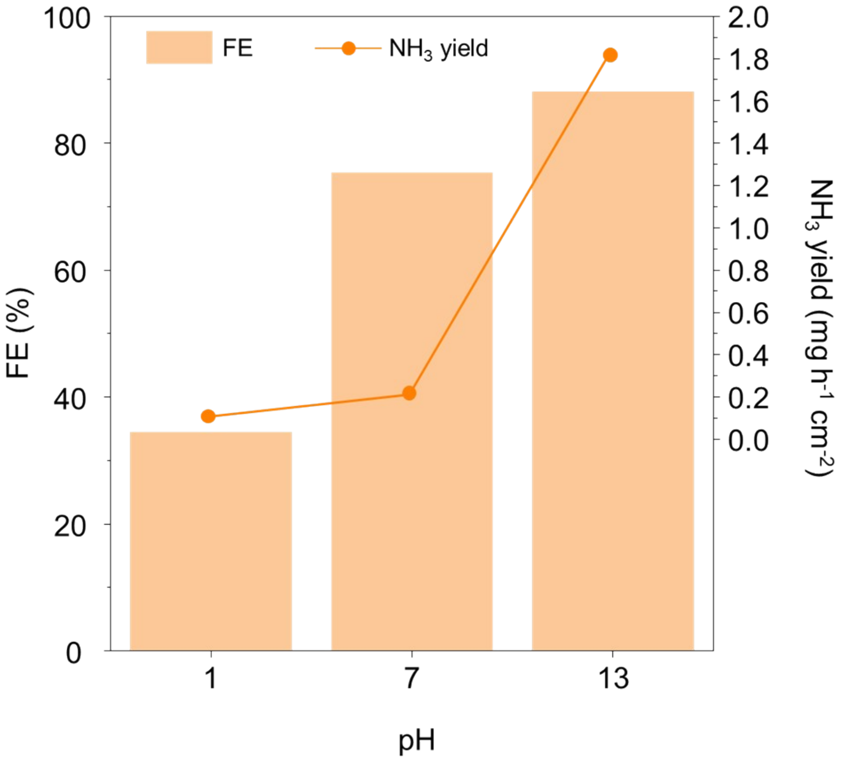

Figure S24. FE and NH_3 yield rates of TU-82-Fe as a function of electrolyte pH, demonstrating catalytic activity across acidic (pH 1), neutral (pH 7), and alkaline (pH 13) conditions.

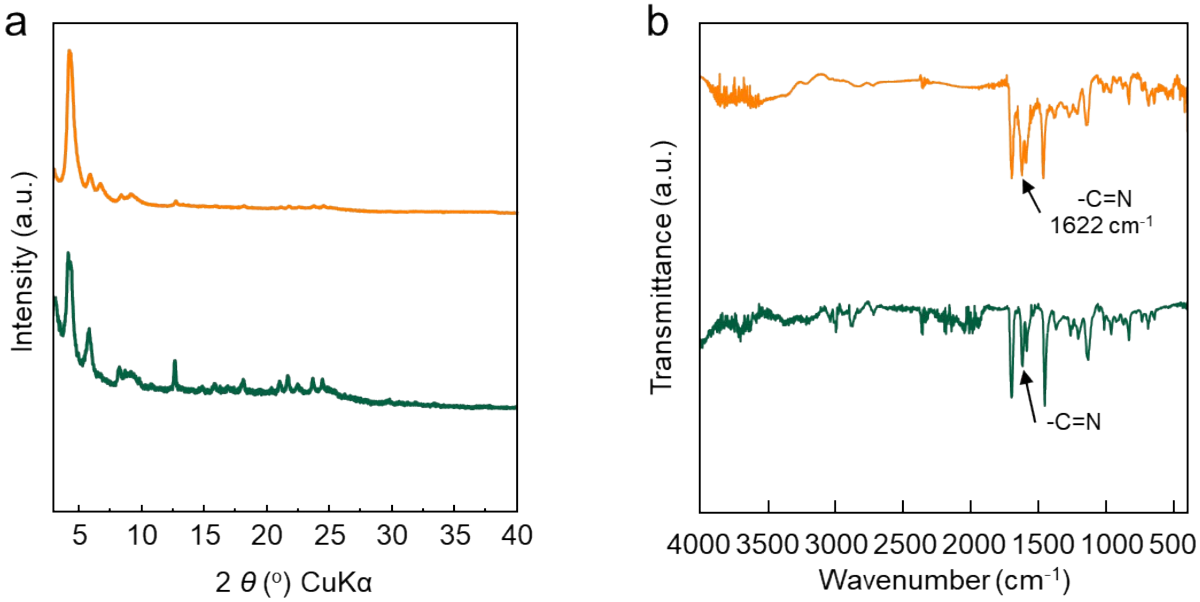

Figure S25. (a) PXRD patterns and (b) FT-IR spectra of TU-82-Fe before (orange) and after (green) NO_3RR.

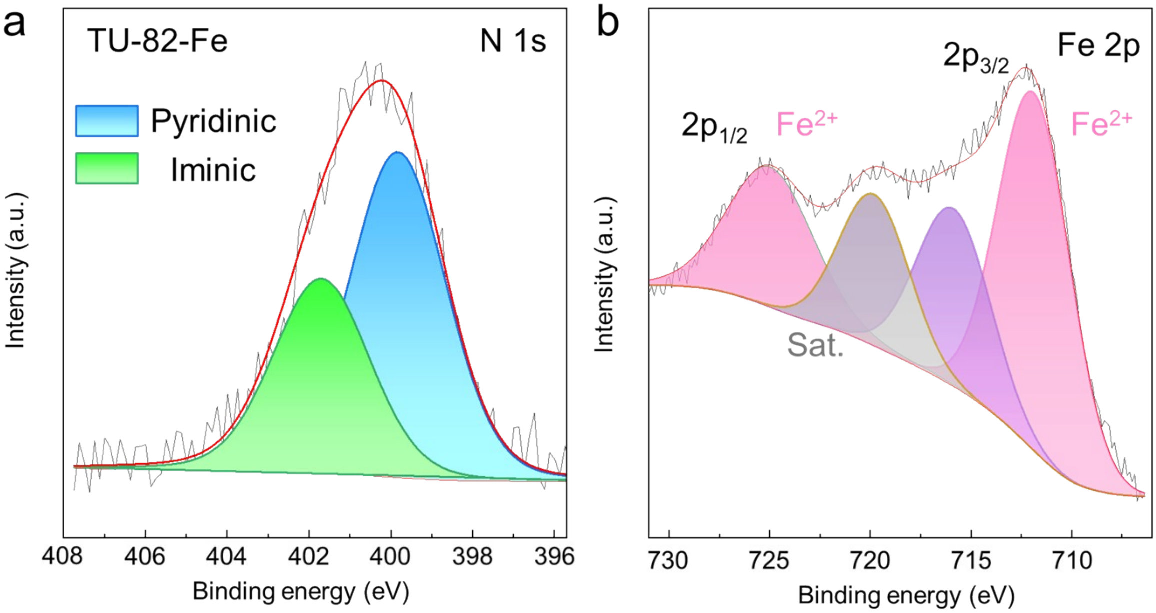

Figure S26. (a) N 1s and (b) Fe 2p XPS spectra of TU-82-Fe after NO_3RR. The N 1s spectrum shows peaks at 399.9 eV (pyridinic N) and 401.7 eV (imine N), consistent with the binding energies observed prior to electrolysis, indicating preservation of the bipyridine coordination environment. The Fe 2p region exhibits characteristic Fe(II) signals at 712.0 eV (Fe $2p_{3/2}$) and 725.1 eV (Fe $2p_{1/2}$), closely matching those of TU-82-Fe before NO_3RR and confirming retention of the Fe(II) oxidation state during NO_3RR. The minor feature between the main 2p peaks originates from background F 1s or O Auger contributions and is not associated with any Fe redox change.

Table S3. Summary of electrocatalytic performance parameters for NO_3RR over TU-82-based and state-of-the-art electrocatalysts.

Catalyst	Electrolyte	FE_{max} (%)	NH_3 yield rate	Overpotential	TOF	Stability	Ref.
COF-366-Fe	0.5 M K_2SO_4 + 0.1 M KNO_3	85.4	1883.6 μmol h^{-1} mg^{-1}_{COF}	−1.7 V vs SCE	-	1 h × 10 times at −1.7 V vs SCE	8
CuPOR-COF	1 M KOH + 1 M KNO_3	~86	6.0 mg h^{-1} cm^{-2}	−1.8 V vs Ag/AgCl	-	15 min × 10 times at −1.7 V vs Ag/AgCl	9
Cu–PTCDA	0.1 M PBS + 500 ppm NO_3^-	85.9	436 ± 85 μg h^{-1} cm^{-2}	−0.4 V vs RHE	-	15 h at −0.4 V vs. RHE	10
Ce MOF–Cu	0.5 M Na_2SO_4 + 5 mM $NaNO_3$	85.5	66 μmol h^{-1} cm^{-2}	−0.9 V vs RHE	219.2 h^{-1}	24 h at −0.9 V *vs* RHE	11
Cu@CuHHTP	0.5 M Na_2SO_4 + 500 ppm NO_3^-	67.55	1.84 mg h^{-1} cm^{-2}	−0.95 V vs RHE	-	2 h × 5 times at −0.95 V vs RHE	12
$Ni_{1.5}Cu_{1.5}(HITP)_2$	0.1 M Na_2SO_4 + 50 mM NO_3^-	72.45	130.93 μmol h^{-1} cm^{-2}	−0.9 V vs RHE	0.653 s^{-1}	30 min × 6 times at −0.9 V vs RHE	13
Cu/Pd/CuO_x	0.5 M K_2SO_4 + 50 ppm NO_3^-	84.04	1510.3 μg h^{-1} $mg^{-1}_{cat.}$	−1.3 V vs SCE	-	2 h × 5 times at −1.3 V vs. SCE	14
ISAA In–Pd	0.5 M Na_2SO_4 + 100 mM NO_3^-	87.2	28.06 mg h^{-1} mg_{Pd}^{-1}	−0.6 V vs RHE	-	100 h × 20 times at −0.6 V vs RHE	15
Cu@Th–BPYDC	1 M KOH + 0.1 M KNO_3	92.5	225.3 μmol h^{-1} cm^{-2}	0 V vs RHE	-	1000 times CV scans	16
OD–Cu foam	1 M KOH + 0.1 M NO_3^-	92	1.1 mmol h^{-1} cm^{-2}	−0.15 V vs RHE	-	30 min × 4 times at −0.15 V vs RHE	17
Cu_2O Nanocubes	0.1 M Na_2SO_4 + 8 mM $NaNO_3$	88 ± 5	7570 ± 473 $μg_{product}$ h^{-1} $mg_{catalyst}^{-1}$	−0.30 V vs RHE	-	-	18
NiPr-TPA-COF	0.5 M K_2SO_4 + 0.1 M KNO_3	90	2.5 mg h^{-1} cm^{-2}	−1.46 V vs SCE	3.5 s^{-1}	30 min × 10 times at −1.38 V vs SCE	19
Fe SAC	0.1 M K_2SO_4 + 0.5 M KNO_3	~75	5245 μg h^{-1} $mg_{cat.}^{-1}$	−0.66 V vs RHE	-	35 h at 35 mA cm^{-2}	20
Cu-N-C SAC	0.1 M KOH + 0.1 M KNO_3	84.7	12.5 mol_{NH3} g^{-1}_{Cu} h^{-1}	−1.0 V vs RHE	-	30 min × 20 times at −1.00 V vs. RHE	21
Cu/SO_3-MOF-808	100 mM $NaNO_3$ + 0.5 M Na_2SO_4	87.5	0.383 mmol/h mg_{cat}	−1.19 V vs SHE	-	-	22
Cu@Cu_{2+1}O NWs	0.5 M K_2SO_4 + 50 ppm NO_3^-	87.07	576.53 μg h^{-1} $mg^{-1}_{cat.}$	−1.2 V vs SCE	-	2 h × 8 times at −1.2 V vs. SCE	23
RuNi–MOF	0.1 M Na_2SO_4 + 50 ppm NO_3^-	~73	274 μg h^{-1} $mg^{-1}_{cat.}$	−1.2 V vs Ag/AgCl	-	1 h × 24 times at −1.6 V vs.Ag/AgCl	24
TU-82-Fe	0.1 M KOH + 0.1 M KNO_3	88.1	2.87 mg h^{-1} cm^{-2}	−0.8 V vs RHE	7.2 h^{-1}	1 h × 10 times at −0.6 V vs RHE	This work

14. Density functional theory (DFT) calculations

Table S4. Calculated electronic energies (E), zero-point energy corrections (ZPE), entropic contributions (T·S), and Gibbs free energies (G = E + ZPE − T·S) of key intermediates involved in the NO_3RR on different single-atom catalytic sites. All values are given in electronvolts (eV). The most stable adsorption configurations of each intermediate were optimized to determine the listed energies.

	E	ZPE	TS	G
TU-82-Cu	-437.286	0.000	0.000	-437.286
NO_3*	-461.543	0.370	0.220	-461.393
NO_2*	-455.852	0.250	0.250	-455.852
NO*	-450.646	0.200	0.120	-450.566
NOH*	-452.959	0.480	0.130	-452.609
N*	-441.274	0.050	0.080	-441.304
NH*	-446.101	0.290	0.120	-445.931
NH_2*	-452.031	0.680	0.100	-451.451
NH_3*	-457.495	1.020	0.130	-456.605
NHO*	-453.625	0.470	0.170	-453.325
NHOH*	-457.786	0.770	0.170	-457.186
NH_2OH*	-462.677	1.150	0.200	-461.727
	E	ZPE	TS	G
TU-82-Fe	-485.919	0.000	0.000	-485.919
NO_3*	-510.425	0.400	0.300	-510.325
NO_2*	-504.814	0.300	0.210	-504.724
NO*	-499.026	0.210	0.080	-498.896
NOH*	-501.649	0.470	0.160	-501.339
N*	-491.322	0.090	0.010	-491.242
NH*	-495.515	0.320	0.100	-495.295
NH_2*	-500.934	0.670	0.100	-500.364
NH_3*	-506.016	1.010	0.160	-505.166
NHO*	-502.426	0.480	0.170	-502.116
NHOH*	-506.459	0.800	0.150	-505.809
NH_2OH*	-511.034	1.160	0.170	-510.044

15. Unit cell information and fractional atomic coordinates

Table S5. Unit cell information and fractional atomic coordinates of TU-82 calculated based on the non-interpenetrated **bcu** topology.

Space group		*Imm2* (No. 44)	
Calculated unit cell		*a* = 17.4656 Å, *b* = 29.2450 Å, *c* = 33.0385 Å, *α* = *β* = *γ* = 90°	
Atoms	x	y	z
C	0.1307	0.0418	0.14294
C	0.14159	0.08694	0.16352
N	0.19936	0.09238	0.80432
C	0.66895	0.32512	0.29299
C	0.71705	0.36317	0.28668
C	0.89795	0.04122	0.89823
C	0.76671	0.65144	0.73116
C	0.14844	0.78521	0.2316
N	0.27924	0.8046	0.24404
C	0.22295	0.77218	0.24398
C	0.64154	0.45818	0.35849
C	0.66009	0.41292	0.33992
N	0.68401	0.40675	0.69775
C	0.13463	0.17005	0.21767
C	0.19455	0.13806	0.21622
C	0.40195	0.45879	0.60127
C	0.28462	0.85694	0.76318
N	0.6905	0.71699	0.2788
C	0.8055	0.68672	0.24856
C	0.7578	0.72452	0.25757
H	0.11595	0.11619	0.14739
H	0.61424	0.32877	0.30901
H	0.91385	0.07296	0.91406
H	0.81356	0.62726	0.73087
H	0.10099	0.76158	0.23287
H	0.07732	0.1603	0.20804
H	0.41665	0.42704	0.58507

H	0.3216	0.88595	0.75713
H	0.8579	0.69036	0.23024
H	0.64205	0.3832	0.35834
C	0.04038	0	0.03872
C	0.16148	0	0.83843
C	0.08256	0	0.918
C	0.95962	0	0.95958
C	0.85194	0	0.16379
C	0.91803	0	0.0805
C	0.08077	0	-0.00082
C	0.16671	0	-0.00073
H	0.19191	0	0.80771
H	0.82768	0	0.19625

16. Supplementary references

(1) B. Ravel, M. Newville, *J. Synchrotron Radiat.* **2005**, *12*, 537–541.

(2) S. I. Zabinsky, J. J. Rehr, A. Ankudinov, R. C. Albers, M. J. Eller, *Phys. Rev. B* **1995**, *52*, 2995−3009.

(3) F. Jin, E. Lin, T. Wang, S. Geng, T. Wang, W. Liu, F. Xiong, Z. Wang, Y. Chen, P. Cheng, Z. Zhang, *J. Am. Chem. Soc.* **2022**, *144*, 5643–5652.

(4) M. Albrecht, I. Janser, A. Lützen, M. Hapke, R. Fröhlich, P. Weis, *Chem. - Eur. J.* **2005**, *11*, 5742–5748.

(5) G. Kresse, D. Joubert, *Phys. Rev. B* **1999**, *59*, 1758–1775.

(6) Y. Huang, J. Long, Y. Wang, N. Meng, Y. Yu, S. Lu, J. Xiao, B. Zhang, *ACS Appl. Mater. Interfaces* **2021**, *13*, 54967–54973.

(7) *CRC Handbook of Chemistry and Physics*, 90th ed., Lide, D. R. (Ed.), CRC Press (Taylor and Francis Group), Boca Raton, FL. 2009.

(8) H. Hu, R. Miao, F. Yang, F. Duan, H. Zhu, Y. Hu, M. Du, S. Lu, *Adv. Energy Mater.* **2024**, *14*, 2302608.

(9) S. I. G. P. Mohamed, S. Namvar, T. Zhang, H. Shahbazi, Z. Jiang, A. M. Rappe, A. Salehi-Khojin, S. Nejati, *Adv. Mater.* **2024**, *36*, 2309302.

(10) G.-F. Chen, Y. Yuan, H. Jiang, S.-Y. Ren, L.-X. Ding, L. Ma, T. Wu, J. Lu, H. Wang, *Nat. Energy* **2020**, *5*, 605–613.

(11) Y.-T. Xu, M.-Y. Xie, H. Zhong, Y. Cao, *ACS Catal.* **2022**, *12*, 8698–8706.

(12) X. Zhu, H. Huang, H. Zhang, Y. Zhang, P. Shi, K. Qu, S.-B. Cheng, A.-L. Wang, Q. Lu, *ACS Appl. Mater. Interfaces* **2022**, *14*, 32176−32182.

(13) J. Yan, J. Li, P. Liu, H. Huang, W. Song, *Green Chem.* **2023**, *25*, 8645−8651.

(14) T. Ren, Z. Yu, H. Yu, K. Deng, Z. Wang, X. Li, H. Wang, L. Wang, Y. Xu, *Appl. Catal., B* **2022**, *318*, 121805.

(15) M. Xie, S. Tang, Z. Li, M. Wang, Z. Jin, P. Li, X. Zhan, H. Zhou, G. Yu, *J. Am. Chem. Soc.* **2023**, *145*, 13957–13967.

(16) Z. Gao, Y. Lai, Y. Tao, L. Xiao, L. Zhang, F. Luo, *ACS Cent. Sci.* **2021**, *7*, 1066−1072.

(17) J. Yuan, Z. Xing, Y. Tang, C. Liu, *ACS Appl. Mater. Interfaces* **2021**, *13*, 52469−52478.

(18) L. Bai, F. Franco, J. Timoshenko, C. Rettenmaier, F. Scholten, H. S. Jeon, A. Yoon, M. Rüscher, A. Herzog, F. T. Haase, S. Kühl, S. W. Chee, A. Bergmann, R. C. Beatriz, *J. Am. Chem. Soc.* **2024**, *146*, 9665–9678.

(19) F. Lv, M. Sun, Y. Hu, J. Xu, W. Huang, N. Han, B. Huang, Y. Li, *Energy Environ. Sci.* **2023**, *16*, 201−209.

(20) Z.-Y. Wu, M. Karamad, X. Yong, Q. Huang, D. A. Cullen, P. Zhu, C. Xia, Q. Xiao, M. Shakouri, F.-Y. Chen, J. Y. Kim, Y. Xia, K. Heck, Y. Hu, M. S. Wong, Q. Li, I. Gates, S. Siahrostami, H. Wang, *Nat. Commun.* **2021**, *12*, 2870.

(21) J. Yang, H. Qi, A. Li, X. Liu, X. Yang, S. Zhang, Q. Zhao, Q. Jiang, Y. Su, L. Zhang, J.-F. Li, Z.-Q. Tian, W. Liu, A. Wang, T. Zhang, *J. Am. Chem. Soc.* **2022**, *144*, 12062−12071.

(22) Y.-S. Tsai, S.-C. Yang, T.-H. Yang, C.-H. Wu, T.-C. Lin, C.-W. Kung, *ACS Appl. Mater. Interfaces* **2024**, *16*, 62185–62194.

(23) T. Ren, K. Ren, M. Wang, M. Liu, Z. Wang, H. Wang, X. Li, L. Wang, Y. Xu, *Chem. Eng. J.* **2021**, *426*, 130759.

(24) J. Qin, K. Wu, L. Chen, X. Wang, Q. Zhao, B. Liu, Z. Ye, *J. Mater. Chem. A* **2022**, *10*, 3963−3969.